Linear analysis of dewetting instability in multilayer planar sheets for composite nanostructures

Bingrui Xu* and Daosheng Deng†
Department of Aeronautics and Astronautics, Fudan University, Shanghai 200433, China

(Received 22 April 2020; accepted 5 August 2020; published 24 August 2020)

Inspired by the recent multifluid system with thickness down to microscopic scale during thermal drawing for fiber fabrication, we perform the linear analysis of dewetting instability in multilayer planar sheets. The effects of various physical parameters on the dewetting instability have been extensively investigated, including van der Waals forces, viscosities, surface tensions, and thicknesses. As the thickness of the liquid sheet is reduced down to nanoscales, van der Waals forces become more prominent and lead to the dewetting instability. For the three-layer case ($N = 3$), the "para-varicose" mode with larger thickness perturbations plays a dominant role. For the four-layer case ($N = 4$), there are several more complicated unstable modes, and the maximum growth rate (Ω_m) depends on both fluid properties, and the corresponding eigenamplitudes can switch among various modes. Particularly, a slowest growth rate (Ω_m^{slow}) is identified at a critical thickness of the cladding layer (H_{cr}). Additionally, for the relevant applications of fiber drawing, by changing multilayer structure from $N = 3$ to 4 through introducing an additional less viscous sheet, the instability can be enhanced, or, by choosing a suitable thickness of a less viscous sheet, the instability can be reduced. These results not only shed light on controlling the dewetting instability by material selection and structure design, but also provide guidance to achieve functional devices with sophisticated nanostructures either in a single fiber or in integrated fabrics for large-scale textiles.

DOI: 10.1103/PhysRevFluids.5.083904

I. INTRODUCTION

Liquid sheets are very common in nature at both small scales (such as tear films in eyes) and large scales (such as the subduction of dense lithosphere into the mantle in geophysics). The breakup of liquid sheets and the subsequent intriguing patterns are essential for many industrial applications including chemical combustion, diesel engines, spray cooling, surface coating, medicine, and microfluidics [1–3]. Oron *et al.* [1] and Craster and Matar [2] extensively reviewed the research on the dynamics and stability of thin liquid sheets. Particularly, the stability and breakup of liquid sheets moving in fluids have been well studied. Dorman [4] and Dombrowski and Fraser [5] experimentally studied the breakup and drop formation of planar sheets. The linear instability of a planar liquid sheet with constant thickness moving in a gas ambient was analyzed by Squire [6] and Hagerty and Shea [7]. It is found that there are two independent modes of unstable waves (an antisymmetric wave or the sinuous mode, and a symmetric wave or the varicose mode). Moreover, sinuous waves are more unstable than varicose waves. Li and Tankin [8] and Rangel and Sirignano [9] presented a more complex picture; the varicose waves have a higher growth rate when the Weber number (the ratio of inertial and interfacial surface tension forces) is small enough [8] or the density ratio is

*brxu@fudan.edu.cn
†dsdeng@fudan.edu.cn

high enough [9]. Brown [10] observed the "curtain coating" process and studied spatial instability of planar sheets experimentally. Lin [11] made a linear temporal and spatial stability analysis of a viscous liquid curtain. Lin *et al.* [12] extended the study to include the effects of an ambient gas. Ibrahim and Akpan [13] presented a fully three-dimensional linear analysis of a plane viscous liquid sheet in an inviscid gas medium. The effect of non-Newtonian behavior and ambient gases of unequal velocities on the instability of a liquid sheet has been also studied [14–17]. Inspired by the multilayer curtain coating, Dyson *et al.* [18] investigated the stability of double-layer liquid sheets under the long-wave assumption and without the surrounding gas effect. Ye *et al.* [19] complemented Dyson's work by including the effect of the surrounding inviscid/viscous gas.

The work cited above studied the instability of a liquid sheet or a double-layer liquid sheet moving in a gas ambient, where the aerodynamic force generated by the relative velocity between gas medium and liquid plays an important role [6,8,9]. Thus, the Navier-Stokes equations are employed in these studies. If the inertia is neglected in the Stokes regime or the liquid sheet is relatively stationary in the medium, the liquid sheet would be stable since capillary forces (surface tension effects) always tend to damp out perturbations on the sheet.

Recently, sophisticated multifluid systems have been extensively studied for thermal drawing, allowing the successful fabrication of micro/nanostructures in fibers and textiles [20–25]. The typical compatible materials for thermal drawing are pairs of polymer/glass [polyethersulfone (PES)/As_2Se_3, and polysulfones (PSU)/Se] together with additional metals and semiconductors, enabling the achievement of versatile functional nanodevices [23]. During the thermal drawing process, a designed preform, which is made of several thin glass sheets sandwiched by cladding polymer, is heated into a viscous state at an elevated temperature and then stretched into an extended fiber under the applied tension. Generally, the thermal drawing process is extremely stable—the typical Rayleigh-Plateau capillary instability is suppressed, which has insufficient time due to the high viscosity (the viscosity of the glass sheet varies from 1 to 10^5 Pa s, and the polymer viscosity is about 10^5 Pa s [26,27]). Hence, the structure and geometry of the cross-section are well preserved from the initial preform with only a simple scaling down in feature sizes, to the final fiber with the designed structure (multilayer cylindrical sheets [20–24], or multilayer planar sheets [25]).

However, the instability of thin sheets during the thermal drawing process could still occur, when the thickness of a thin film is further reduced drawn to nanometer scales (multilayer cylindrical sheets [26,28], multilayer planar sheets [29]). As the thickness of the As_2Se_3 sheet in the PES/As_2Se_3/PES structure is drawn to less than 10 nm, the As_2Se_3 sheet evolves into an array of continuous filaments arranged orderly (for PSU/Se/PSU, Se sheet thickness less than 100 nm), leading to an intriguing filamentation instability [28,29].

For the typical parameters in the filamentation instability, the associated Reynolds number is $\mathrm{Re} \ll 1$ [26,28]. Then the capillary instability with "aerodynamic force" (the relative velocity between viscous film and polymer layer) for a planar sheet [6] is irrelevant for the observed instability, and another destabilizing factor should be considered. It is noted that the initial thickness of thin films is decreased down to hundreds of nanometers during the thermal drawing process and becomes reminiscent of the spinodal dewetting phenomenon. In the dewetting regime, a liquid film is subjected to dewetting and breaks up below a critical thickness. De Gennes *et al.* [30] discussed and summarized different kinds of dewetting phenomena. For thin films (thickness smaller than 1 μm), long-range forces (van der Waals forces considered in our paper) play a prominent role, resulting in spinodal dewetting. Consequently, a liquid sheet on a solid/liquid substrate spontaneously ruptures into a random array of droplets driven by spinodal dewetting instability (solid substrate by Reiter [31,32], Brochard-Wyart *et al.* [33], Sharma *et al.* [34], Reiter *et al.* [35]; liquid substrate by Brochard-Wyart *et al.* [36]).

Therefore, a physical mechanism of this filamentation instability has been proposed to consider both van der Waals forces and stretching effect using a simplified model of a stretching three-layer fiber (a thin sheet sandwiched between the same surrounding viscous fluids), and the theoretical results agree with experiments remarkably [37]. This theory is mainly based on two assumptions. One assumption is "planar sheets": during the thermal drawing, thickness of the sandwiched thin

sheets is much smaller than the radii (the radii of interfaces are of centimeter scale at the inlet, while the thickness of a thin sheet is less than 10 μm and the stretching length is larger than 10 cm [26,28]), and the multilayer cylindrical sheets can be assumed as multilayer planar sheets by neglecting curvature effect to focus on the dewetting instability. The other is "infinity outermost layers": the outermost high viscous polymer layers are much thicker than the sandwiched thin sheets, and two outermost polymer layers can be assumed extending to infinity as surrounding fluids.

To thoroughly understand the instability of the composite nanostructures, it is necessary to study the instability for multilayer or multifluid systems during thermal drawing. The designed multilayer fiber is drawn over a length from velocity U_0 to the take-up speed U_f. Following the method in [37,38], the total growth of perturbations can be obtained by integrating the local perturbation growth rate along the whole stretching region. Thus, the dewetting instability of a multilayer fiber flowing at a velocity U is indispensable before combining the stretching effect. Mathematically, under the aforementioned assumptions of planar sheets and infinity outermost layers [37], a N-layer fiber can be simplified to a model of N-layer planar sheets, where $(N-2)$ layer thin sheets are sandwiched by the first and Nth layer fluids as surrounding fluids.

In this paper, the linear analysis of dewetting instability is further generalized to be practicable for multilayer planar sheets with arbitrary thicknesses, viscosities, densities, and surface tensions. In Sec. II, a mathematical model of linear analysis for the N-layer viscous fluids problem is presented. In Sec. III, the model is validated by comparing to known analytical results of previous work. Then three-layer and multilayer problems are thoroughly discussed in Secs. IV and V, respectively. In Sec. VI, the application of controlling dewetting instability (e.g., suppressing or enhancing the instability) for fiber drawing is explored. We conclude with an outlook in the last section for future work on dewetting instability in the composite nanostructures.

II. MATHEMATICAL MODEL

A. Governing equations and interfacial conditions

Here we consider two-dimensional multifluid sheets. The coordinates are chosen so that the z axis is parallel to the direction of the liquid sheet flow, and the y axis is parallel to the thickness, with its origin located at the middle plane as shown in Fig. 1. The total number of viscous fluid layers is N, the viscosity of the jth layer is μ_j, and its thickness is H_j with the subscript $j = 1, 2, \ldots, N$ denoting the jth layer. The first $(j = 1)$ layer and the Nth layer are the outermost ones (much thicker than sandwiched thin sheets, assumed extending to infinity), so we set $H_1 = H_N = +\infty$. The governing equations of this flow are

$$\frac{\partial \boldsymbol{u}_j}{\partial t} + (\boldsymbol{u}_j \cdot \nabla)\boldsymbol{u}_j = -\frac{1}{\rho_j}\nabla p_j + \frac{1}{\rho_j}\nabla \cdot \boldsymbol{\tau}_j, \tag{1}$$

$$\nabla \cdot \boldsymbol{u}_j = 0, \tag{2}$$

where the velocity $\boldsymbol{u}_j = (v_j, w_j)$, $\nabla = (\partial/\partial y, \partial/\partial z)$, p_j is the pressure, ρ_j is the density, and $\boldsymbol{\tau}_j = \mu_j[\nabla \boldsymbol{u}_j + (\nabla \boldsymbol{u}_j)^T]$ is the viscous shear stress tensor.

The solutions of the above equations satisfy the interfacial coupling conditions on the interfaces $y = Y^{(i)}(z, t)$, where the superscript $1 \leqslant i \leqslant N-1$ means the ith interface between the i and $i+1$ fluid layers, i.e., the thickness $H_{i+1} = Y^{(i+1)} - Y^{(i)}$. The unit normal vector and the unit tangential vectors at the ith interface are $\boldsymbol{n}^{(i)}$ and $\boldsymbol{t}^{(i)}$, respectively. Four interfacial coupling conditions are as below: the first two are kinematic conditions, while the last two are dynamic conditions. First, the velocity component normal to the interface is continuous across the interface, i.e.,

$$\boldsymbol{n}^{(i)} \cdot \boldsymbol{u}_i = \boldsymbol{n}^{(i)} \cdot \boldsymbol{u}_{i+1} = \frac{DY^{(i)}}{Dt} = \frac{\partial Y^{(i)}}{\partial t} + (\boldsymbol{u}_i \cdot \nabla)Y^{(i)} \quad \text{at } y = Y^{(i)}(z, t). \tag{3}$$

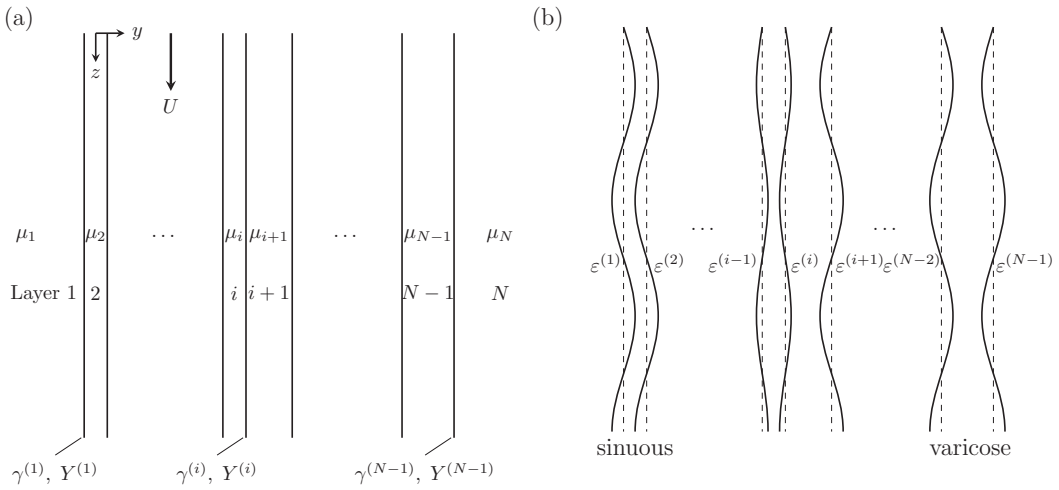

FIG. 1. Schematic of the multilayer planar sheets. (a) N layers and corresponding interfaces $Y^{(i)}$, viscosities μ_i, and interfacial tensions $\gamma^{(i)}$ with perfect parallel geometry. (b) Small perturbations are introduced to analyze their growth with linear stability analysis, here sinuous mode perturbation in the second layer (or at the first and second interface), while varicose mode perturbation in the $(N-1)$th layer [or at the $(N-2)$th and $(N-1)$th interface].

Second, the tangential component of the velocity is continuous at the interface due to the no-slip condition:

$$\boldsymbol{u}_i \cdot \boldsymbol{t}^{(i)} = \boldsymbol{u}_{i+1} \cdot \boldsymbol{t}^{(i)} \quad \text{at } y = Y^{(i)}(z,t). \tag{4}$$

Third, the tangential stress of the liquid sheet should be continuous at the interfaces:

$$\boldsymbol{n}^{(i)} \cdot \boldsymbol{\tau}_i \cdot \boldsymbol{t}^{(i)} = \boldsymbol{n}^{(i)} \cdot \boldsymbol{\tau}_{i+1} \cdot \boldsymbol{t}^{(i)} \quad \text{at } y = Y^{(i)}(x,z,t). \tag{5}$$

Finally, the normal surface stresses on both sides of the interface, including the pressure jump across the interface due to surface tension, are balanced:

$$p_i - \boldsymbol{n}^{(i)} \cdot (\boldsymbol{\tau}_i - \boldsymbol{\tau}_{i+1}) \cdot \boldsymbol{n}^{(i)} - p_{i+1} = \gamma^{(i)}\kappa^{(i)} - \frac{dV(H_{i+1})}{dH_{i+1}} + \frac{dV(H_i)}{dH_i} \quad \text{at } y = Y^{(i)}(z,t), \tag{6}$$

where $\kappa^{(i)}(x,z,t)$ is the mean curvature of the interface and can be calculated directly from the vector $\boldsymbol{n}^{(i)}$ of the interface by $\kappa^{(i)} = \boldsymbol{\nabla} \cdot \boldsymbol{n}^{(i)}$. The van der Waals forces from the ith layer can be introduced by the potential energy per unit area $V(H_i)$ as a function of thickness H_i. A typical representation for the potential V_i is given with a Hamaker constant A_i [30]:

$$V(H_i) = -\frac{A_i}{12\pi H_i^2}. \tag{7}$$

Since van der Waals forces are long-range intermolecular forces and decay rapidly with distances, for each interface, only the interactions with its two nearest interfaces are considered to simplify the model.

B. Primary flow in steady state

In the steady state, due to the no-slip interfacial conditions of viscous fluids, all layers of fluids flow downstream at a constant velocity $\bar{\boldsymbol{u}}_j = (0, U)$. Consequently, the stress tensors in steady state are also $\bar{\boldsymbol{\tau}}_j = \boldsymbol{0}$. The interfaces of the planar multifluid sheet in the steady state are parallel to the

z direction at $y = Y^{(i)}$. Thus, the corresponding normal and tangential vectors are $\bar{\boldsymbol{n}}^{(i)} = (1, 0)$ and $\bar{\boldsymbol{t}}^{(i)} = (0, 1)$.

C. Perturbed state

To carry out a linear stability analysis, this state is disturbed by small perturbations. The dependent variables, for example, the pressures, velocities, and gas-liquid interface, can each be presented as the sum of the value found in the undisturbed steady state plus the unsteady perturbation:

$$\begin{bmatrix} \boldsymbol{u}_j \\ p_j \\ \boldsymbol{\tau}_j \\ Y^{(i)} \\ \boldsymbol{n}^{(i)} \\ \boldsymbol{t}^{(i)} \end{bmatrix} = \begin{bmatrix} \bar{\boldsymbol{u}}_j \\ \bar{p}_j \\ \bar{\boldsymbol{\tau}}_j \\ \bar{Y}^{(i)} \\ \bar{\boldsymbol{n}}^{(i)} \\ \bar{\boldsymbol{t}}^{(i)} \end{bmatrix} + \begin{bmatrix} \tilde{\boldsymbol{u}}_j \\ \tilde{p}_j \\ \tilde{\boldsymbol{\tau}}_j \\ \tilde{Y}^{(i)} \\ \tilde{\boldsymbol{n}}^{(i)} \\ \tilde{\boldsymbol{t}}^{(i)} \end{bmatrix}. \tag{8}$$

Substituting Eq. (8) into the governing equations (1) and (2) and the boundary conditions (3)–(6), the following linearized equations are obtained by neglecting the nonlinear terms:

$$\frac{\partial \tilde{\boldsymbol{u}}_j}{\partial t} + U\frac{\partial \tilde{\boldsymbol{u}}_j}{\partial z} = -\frac{1}{\rho_j}\nabla \tilde{p}_j + \frac{\mu_j}{\rho_j}\nabla^2 \tilde{\boldsymbol{u}}_j, \tag{9}$$

$$\nabla \cdot \tilde{\boldsymbol{u}}_j = 0, \tag{10}$$

$$\tilde{\boldsymbol{u}}_i \cdot \bar{\boldsymbol{n}}^{(i)} = \tilde{\boldsymbol{u}}_{i+1} \cdot \bar{\boldsymbol{n}}^{(i)} = \frac{\partial \tilde{Y}^{(i)}}{\partial t} \quad \text{at } y = \bar{Y}^{(i)}(x, z, t), \tag{11}$$

$$\tilde{\boldsymbol{u}}_i \cdot \bar{\boldsymbol{t}}^{(i)} = \tilde{\boldsymbol{u}}_{i+1} \cdot \bar{\boldsymbol{t}}^{(i)} \quad \text{at } y = \bar{Y}^{(i)}(x, z, t), \tag{12}$$

$$\bar{\boldsymbol{n}}^{(i)} \cdot \tilde{\boldsymbol{\tau}}_i \cdot \bar{\boldsymbol{t}}^{(i)} = \bar{\boldsymbol{n}}^{(i)} \cdot \tilde{\boldsymbol{\tau}}_{i+1} \cdot \bar{\boldsymbol{t}}^{(i)} \quad \text{at } y = \bar{Y}^{(i)}(x, z, t), \tag{13}$$

$$\tilde{p}_i - \bar{\boldsymbol{n}}^{(i)} \cdot (\tilde{\boldsymbol{\tau}}_i - \tilde{\boldsymbol{\tau}}_{i+1}) \cdot \bar{\boldsymbol{n}}^{(i)} - \tilde{p}_{i+1} = -\gamma^{(i)}\frac{\partial^2 \tilde{Y}^{(i)}}{\partial z^2} + \frac{A_{i+1}\tilde{H}_{i+1}}{2\pi H_{i+1}^4} - \frac{A_i \tilde{H}_i}{2\pi H_i^4} \quad \text{at} \quad y = \bar{Y}^{(i)}(z, t). \tag{14}$$

Here $\tilde{\kappa}^{(i)} = \nabla \cdot \tilde{\boldsymbol{n}}^{(i)} = -\partial^2 \tilde{Y}^{(i)}/\partial z^2$ is used in the last interfacial coupling condition (14). Moreover, according to the condition (14) the perturbations of van der Waals forces are proportional to $1/H^4$, therefore it is reasonable to only consider the interactions with its two nearest interfaces for each interface [the interaction between $(i-2)$th and ith interfaces proportional to $1/(H_{i-1} + H_i)^4$ is much smaller, about $0.0625 \times (1/H_i^4)$ at $H_{i-1} \sim H_i$].

D. Dispersion relation

To solve Eqs. (9)–(14), the stream function $\tilde{\phi}_j$ is introduced here:

$$\tilde{v}_j = -\frac{\partial \tilde{\phi}_j}{\partial z}, \quad \tilde{w}_j = \frac{\partial \tilde{\phi}_j}{\partial y}. \tag{15}$$

Substituting the stream function (15) into the linearized equation (9) and then eliminating the pressure term yields the following equation:

$$\nabla^2\left(\nabla^2 - \frac{\rho_j}{\mu_j}\frac{\partial}{\partial t}\right)\tilde{\phi}_j = 0. \tag{16}$$

In linear instability analysis, the perturbations are in the form $\exp^{\sigma t+ikz}$, where a real number k is the perturbation wave number and the real part of σ is the exponential growth rate ω, i.e., $\omega = \mathrm{Re}(\sigma)$. Substituting $\tilde{\phi}_j = \tilde{\Phi}_j \exp^{\sigma t+ikz}$ into Eq. (16) yields

$$\left(\frac{d^2}{dz^2} - k^2\right)\left(\frac{d^2}{dz^2} - l_j^2\right)\tilde{\Phi}_j = 0, \tag{17}$$

where $l_j^2 = k^2 + \rho_j(\sigma + ikU)/\mu_j$. Thus, the general solution of Eq. (17) is

$$\tilde{\Phi}_j = c_{1,j}e^{ky} + c_{2,j}e^{-ky} + c_{3,j}e^{l_j y} + c_{4,j}e^{-l_j y}. \tag{18}$$

Then, the velocity of perturbations becomes

$$\tilde{\boldsymbol{u}}_j = \begin{bmatrix}\tilde{v}_j \\ \tilde{w}_j\end{bmatrix} = \begin{bmatrix}\tilde{V}_j \\ \tilde{W}_j\end{bmatrix} e^{(\sigma t+ikz)} = \begin{bmatrix} ik(c_{1,j}e^{ky} + c_{2,j}e^{-ky} + c_{3,j}e^{l_j y} + c_{4,j}e^{-l_j y}) \\ -k(c_{1,j}e^{ky} - c_{2,j}e^{-ky}) - l_j(c_{3,j}e^{l_j y} - c_{4,j}e^{-l_j y})\end{bmatrix} e^{(\sigma t+ikz)}. \tag{19}$$

Then the pressure can also be obtained from the z-component momentum equation:

$$\tilde{p}_j = -i\rho_j\sigma_U(c_{1,j}e^{ky} - c_{2,j}e^{-ky})e^{(\sigma t+ikz)}, \tag{20}$$

where $\sigma_U = (\sigma + ikU)$.

The integral constants $c_{1,j}, c_{2,j}, c_{3,j}, c_{4,j}$ can be solved by substituting the velocity and pressure expressions (19) and (20) into the interfacial coupling conditions (11)–(14). After some algebraic manipulation, the linear equation set about these integral constants can be transformed into the matrix form:

$$\left[\boldsymbol{A}_{i,i} - \frac{1}{\sigma}\left(\gamma^{(i)}k^2 - \frac{A_i}{2\pi H_i^4} - \frac{A_{i+1}}{2\pi H_{i+1}^4}\right)\boldsymbol{B}_i\right]\boldsymbol{c}_i - \left(\boldsymbol{A}_{i,i+1} + \frac{1}{\sigma}\frac{A_{i+1}}{2\pi H_{i+1}^4}\boldsymbol{B}_{i+1}\right)\boldsymbol{c}_{i+1} - \frac{1}{\sigma}\frac{A_i}{2\pi H_i^4}\boldsymbol{B}_{i-1}\boldsymbol{c}_{i-1} = 0, \tag{21}$$

where $\boldsymbol{c}_i = (c_{1,i}, c_{2,i}, c_{3,i}, c_{4,i})^T$. Additionally, $\boldsymbol{A}_{i,j}$ and $\boldsymbol{B}_i$ are 4×4 matrices as below:

$$\boldsymbol{A}_{i,j} = \begin{bmatrix} e^{kY^{(i)}} & e^{-kY^{(i)}} & e^{l_j Y^{(i)}} & e^{-l_j Y^{(i)}} \\ ke^{kY^{(i)}} & -ke^{-kY^{(i)}} & l_j e^{l_j Y^{(i)}} & -l_j e^{-l_j Y^{(i)}} \\ 2\mu_j k^2 e^{kY^{(i)}} & 2\mu_j k^2 e^{-kY^{(i)}} & \mu_j\left(k^2 + l_j^2\right)e^{l_j Y^{(i)}} & \mu_j\left(k^2 + l_j^2\right)e^{-l_j Y^{(i)}} \\ -(i\rho_j\sigma_U + 2ik^2\mu_j)e^{kY^{(i)}} & (i\rho_j\sigma_U + 2ik^2\mu_j)e^{-kY^{(i)}} & -2ikl_j\mu_j e^{l_j Y^{(i)}} & 2ikl_j\mu_j e^{-l_j Y^{(i)}} \end{bmatrix}, \tag{22}$$

$$\boldsymbol{B}_i = ik\begin{bmatrix} 0 & 0 & 0 & 0 \\ 0 & 0 & 0 & 0 \\ 0 & 0 & 0 & 0 \\ e^{kY^{(i)}} & e^{-kY^{(i)}} & e^{l_i Y^{(i)}} & e^{-l_i Y^{(i)}} \end{bmatrix}. \tag{23}$$

Expanding the matrix equation (21) to all the $N-1$ interfaces yields the final matrix equation

$$\boldsymbol{M}^{(N)}\boldsymbol{C} = \boldsymbol{0}, \tag{24}$$

for the integral constants vector $\boldsymbol{C} = (c_{1,1}, c_{3,1}, \boldsymbol{c}_2^T, \boldsymbol{c}_3^T, \ldots, \boldsymbol{c}_{N-1}^T, c_{2,N}, c_{4,N})^T$, where the matrix $\boldsymbol{M}^{(N)}$ is a $4N \times 4N$ matrix as

$$\boldsymbol{M}^{(N)} = \boldsymbol{M}_1^{(N)} - \frac{1}{\sigma}\boldsymbol{M}_2^{(N)} = \begin{bmatrix} \tilde{\boldsymbol{A}}_{1,1} & -\boldsymbol{A}_{1,2} & & & & & \\ & \boldsymbol{A}_{2,2} & -\boldsymbol{A}_{2,3} & & & & \\ & & \ddots & \ddots & & & \\ & & & \boldsymbol{A}_{N-2,N-2} & -\boldsymbol{A}_{N-2,N-1} & & \\ & & & & \boldsymbol{A}_{N-1,N-1} & -\tilde{\boldsymbol{A}}_{N-1,N} \end{bmatrix}$$

$$- \frac{1}{\sigma}\begin{bmatrix} b^1\tilde{\boldsymbol{B}}_1 & a_2\boldsymbol{B}_2 & & & & & \\ a_2\tilde{\boldsymbol{B}}_1 & b^2\boldsymbol{B}_2 & a_3\boldsymbol{B}_3 & & & & \\ & & \ddots & \ddots & & & \\ & & a_{N-2}\boldsymbol{B}_{N-3} & b^{N-2}\boldsymbol{B}_{N-2} & a_{N-1}\boldsymbol{B}_{N-1} & & \\ & & & a_{N-1}\boldsymbol{B}_{N-2} & b^{N-1}\boldsymbol{B}_{N-1} & a_N\tilde{\boldsymbol{B}}_N \end{bmatrix}, \tag{25}$$

where $a_i = A_i/(2\pi H_i^4)$ and $b^i = (\gamma^{(i)}k^2 - a_i - a_{i+1})$. Since the first layer and last layer fluids extend to infinity, we have $a_1 = 0$ and $a_N = 0$. Moreover, there is one more boundary condition that perturbations of velocity and pressure should be finite at $y \to -\infty$ and $+\infty$, i.e., $c_{2,1} = c_{4,1} = c_{1,N} = c_{3,N} = 0$. Therefore, $\tilde{\boldsymbol{A}}_{1,1}$ and $\tilde{\boldsymbol{B}}_1$ are the first and third columns of $\boldsymbol{A}_{1,1}$ and $\boldsymbol{B}_1$, and $\tilde{\boldsymbol{A}}_{N-1,N}$ and $\tilde{\boldsymbol{B}}_N$ are the second and fourth columns of $\boldsymbol{A}_{N-1,N}$ and $\boldsymbol{B}_1$.

To obtain a nonzero solution of $\boldsymbol{C}$, the coefficient matrix $\boldsymbol{M}^{(N)}$ should be singular:

$$\det(\boldsymbol{M}^{(N)}) = 0. \tag{26}$$

This root-finding problem can be transformed to an eigenvalue problem by exploiting the matrix structure of $\boldsymbol{M}$:

$$\boldsymbol{M} \cdot \boldsymbol{C} = \boldsymbol{0} \Longleftrightarrow \boldsymbol{M}_2(k, \sigma) \cdot \boldsymbol{C} = \sigma \boldsymbol{M}_1(k, \sigma) \cdot \boldsymbol{C}. \tag{27}$$

Since there is an unknown σ in l_i, the coefficient matrices $\boldsymbol{M}_1$ and $\boldsymbol{M}_2$ are dependent on both k and σ, i.e., they cannot be calculated at a given wave number k. This kind of eigenmatrix equation is called the "nonlinear eigenproblem," and some numerical iteration methods have been built to solve this problem [39–43].

E. Simplification for Stokes problems

For Stokes problems, the linearized momentum equation (9) is simplified by the one without the inertia term (including the time derivative term):

$$\nabla \tilde{p}_j = \mu_j \nabla^2 \tilde{\boldsymbol{u}}_j. \tag{28}$$

Other linearized equations [Eqs. (10)–(14)] still work for Stokes problems. By substituting the stream function $\tilde{\Phi}$, the ordinary difference equation (17) would be

$$\left(\frac{d^2}{dz^2} - k^2\right)^2 \tilde{\Phi}_j = 0. \tag{29}$$

Thus, the solutions of Eq. (29) are

$$\tilde{\Phi}_j = c_{1,j}e^{ky} + c_{2,j}e^{-ky} + c_{3,j}ye^{ky} + c_{4,j}ye^{-ky}. \tag{30}$$

Then similarly, the velocity perturbations

$$\tilde{\boldsymbol{u}}_j = \begin{bmatrix} \tilde{v}_j \\ \tilde{w}_j \end{bmatrix} = \begin{bmatrix} \tilde{V}_j \\ \tilde{W}_j \end{bmatrix} e^{(\sigma t + ikz)}$$
$$= \begin{bmatrix} ik(c_{1,j}e^{ky} + c_{2,j}e^{-ky} + c_{3,j}ye^{ky} + c_{4,j}ye^{-ky}) \\ -(kc_{1,j} + c_{3,j} + kyc_{3,j})e^{ky} - (-kc_{2,j} + c_{4,j} - kyc_{4,j})e^{-ky} \end{bmatrix} e^{(\sigma t + ikz)}. \tag{31}$$

The pressure perturbation can be obtained as

$$\tilde{p}_j = 2\mu_j ik(c_{3,j}e^{ky} + c_{4,j}e^{-ky})e^{(\sigma t + ikz)}. \tag{32}$$

After substituting Eqs. (19) and (20) into the interfacial coupling conditions (11)–(14) and rewriting in matrix form, we can obtain the same determinant equation (26) but the matrices $\boldsymbol{A}_{i,j}$ and $\boldsymbol{B}_i$ are

$$\boldsymbol{A}_{i,j} = \begin{bmatrix} e^{kY^{(i)}} & e^{-kY^{(i)}} & Y^{(i)}e^{kY^{(i)}} & Y^{(i)}e^{-kY^{(i)}} \\ ke^{kY^{(i)}} & -ke^{-kY^{(i)}} & (1+kY^{(i)})e^{kY^{(i)}} & (1-kY^{(i)})e^{-kY^{(i)}} \\ \mu_j k^2 e^{kY^{(i)}} & \mu_j k^2 e^{-kY^{(i)}} & \mu_j k(1+kY^{(i)})e^{kY^{(i)}} & -\mu_j k(1-kY^{(i)})e^{-kY^{(i)}} \\ -2\mu_j ik^2 e^{kY^{(i)}} & 2\mu_j ik^2 e^{-kY^{(i)}} & -2\mu_j ik^2 Y^{(i)}e^{kY^{(i)}} & 2\mu_j ik^2 Y^{(i)}e^{-kY^{(i)}} \end{bmatrix}, \tag{33}$$

$$\boldsymbol{B}_i = ik \begin{bmatrix} 0 & 0 & 0 & 0 \\ 0 & 0 & 0 & 0 \\ 0 & 0 & 0 & 0 \\ e^{kY^{(i)}} & e^{-kY^{(i)}} & Y^{(i)}e^{kY^{(i)}} & Y^{(i)}e^{-kY^{(i)}} \end{bmatrix}. \tag{34}$$

The expressions (33) and (34) could also be deduced from Eqs. (22) and (23) of matrices $\boldsymbol{A}_{i,j}$ and $\boldsymbol{B}_i$ for Navier-Stokes flow by taking the limit $\rho_j \to 0$. The straightforward substitution of $\rho_j = 0$ in (22) and (23) yields dependent columns (the third column corresponding to the first column, the fourth column corresponding to the second column). To avoid this problem, we could adopt the difference between the corresponding two columns in the limit $l_j \to k$, i.e., their derivatives with respect to l_j of third and fourth columns at $l_j = k$, such as $d(e^{l_j Y^i})/dl_j|_{l_j=k} = Y^i e^{kY^i}$. This procedure is equivalent to the one suggested by Tomotika [44].

It is different from the Navier-Stokes problem in that the matrices $\boldsymbol{A}_{i,j}$ and $\boldsymbol{B}_i$ for the Stokes problem are only dependent on the wave number k, as well as the matrices $\boldsymbol{M}_1$ and $\boldsymbol{M}_2$ consequently. And then the nonlinear eigenvalue problem (27) can be simplified to a generalized eigenvalue problem:

$$\boldsymbol{M}_2(k) \cdot \boldsymbol{C} = \sigma \boldsymbol{M}_1(k) \cdot \boldsymbol{C}. \tag{35}$$

Here the matrix $\boldsymbol{M}_1(k)$ is nonsingular, so this generalized eigenvalue problem is typically well conditioned and can be solved via available numerical methods in LAPACK [45]. LAPACK has been incorporated into many current mathematical softwares; the generalized eigenvalue problem (35) can be solved directly for a given wave number k. Since the Reynolds number $\mathrm{Re} \ll 1$ [26,28] in the filamentation instability, Eqs. (25) and (33)–(35) for Stokes problems are used in Secs. IV and V for simplicity.

F. The eigenamplitude and most unstable mode

The generalized eigenvalue problem (35) has $N-1$ roots $\sigma_n(k)$ $(n = 1, 2, \ldots, N-1)$. For each root σ_n, the integral constants vector $\boldsymbol{C}$ is obtained from Eq. (26), and then the initial perturbation amplitudes $\varepsilon^{(i)}$ $(\tilde{Y}^{(i)} = \varepsilon^{(i)}\exp^{\sigma t + ikz})$ on the ith interface can be calculated by $\varepsilon^{(i)} = \tilde{V}_i/\sigma_n$ from Eqs. (11) and (19). The initial perturbation amplitudes of all interfaces are described by a vector $\boldsymbol{\varepsilon} = [\varepsilon^{(1)}, \varepsilon^{(2)}, \ldots, \varepsilon^{(N-1)}]$ ($\boldsymbol{\varepsilon}$ is normalized to $\|\boldsymbol{\varepsilon}\| = 1$), which is called the "eigenamplitudes" of frequency σ_n [27].

The growth rate of perturbations is the real part $\omega_n = \mathrm{Re}(\sigma_n)$. If the growth rate $\omega_n > 0$, then the mode is unstable. For a wave number k, there are $(N-1)$ growth rates for a N-layer problem. It is assumed the instability is dominated by the maximum growth rate, $\omega_m = \max_{n,k}(\omega_n(k))$, called the most unstable mode. And the corresponding wave number and eigenamplitudes are k_m and $\boldsymbol{\varepsilon}_m = (\varepsilon_m^{(1)}, \varepsilon_m^{(2)}, \ldots, \varepsilon_m^{(N-1)})$, respectively.

The growth rate ω_n depends on the viscosity μ_j, the thickness H_j, the Hamaker number A_j, the interfacial tension $\gamma^{(i)}$, and the wave number k. According to the Buckingham π theorem [46], dimensionless growth $\Omega_n = \mathrm{fct}(\eta_j, H_j/H_2, \alpha_j, \lambda^{(i)}, K)$ where

$$\Omega_n = \frac{\omega_n \mu_2 H_2}{\gamma^{(1)}}, \quad \eta_j = \frac{\mu_j}{\mu_2}, \quad \alpha_j = \frac{A_j}{2\pi H_2^2 \gamma^{(1)}}, \quad \lambda^{(i)} = \frac{\gamma^{(i)}}{\gamma^{(1)}}, \quad K = kH_2. \tag{36}$$

η_j is the viscosity ratio, α_j is the ratio of van der Waals forces to interfacial tension, $\lambda^{(i)}$ is the interfacial tension ratio, and K is the dimensionless wave number.

III. MODEL VALIDATION

In this section, our N-layer linear instability model is compared with known analytical results in various cases derived by other researchers as a check validation. At $N = 3$ and the same surrounding fluids $\mu_1 = \mu_3$, $\gamma^{(1)} = \gamma^{(2)}$, the determinant equation (26) has two solutions:

$$\begin{vmatrix} 1 & 1 & 1 & 1 \\ k & l_1 & -k\coth(kH_2/2) & -l_2\coth(l_2H_2/2) \\ 2\mu_1 k^2 & \mu_1(k^2+l_1^2) & 2\mu_2 k^2 & \mu_2(k^2+l_2^2) \\ F_1 & F_2 & F_3\coth(kH_2/2) & F_4\coth(l_2H_2/2) \end{vmatrix} = 0 \tag{37}$$

for the varicose mode, and

$$\begin{vmatrix} 1 & 1 & 1 & 1 \\ k & l_1 & -k\tanh(kH_2/2) & -l_2\tanh(l_2H_2/2) \\ 2\mu_1 k^2 & \mu_1(k^2+l_1^2) & 2\mu_2 k^2 & \mu_2(k^2+l_2^2) \\ F_1 & F_2 & F_3\tanh(kH_2/2) & F_4\tanh(l_2H_2/2) \end{vmatrix} = 0 \tag{38}$$

for the sinuous mode, where

$$F_1 = -\left(\rho_1\sigma_U^2 + 2\mu_1 k^2\sigma_U + \gamma^{\mathrm{eff}}k^3\right), \quad F_2 = -(2\mu_1 k l_1\sigma_U + \gamma^{\mathrm{eff}}k^3),$$
$$F_3 = \left(\rho_2\sigma_U^2 + 2\mu_2 k^2\sigma_U\right), \quad F_4 = 2\mu_2 k l_2\sigma_U, \quad \gamma^{\mathrm{eff}} = \gamma^{(1)} - \frac{A_2}{k^2\pi H_2^4}.$$

Since the perturbed sheet thickness keeps constant for the same surrounding fluids case at $N = 3$ in sinuous mode, the van der Waals interaction term in γ^{eff} would disappear, i.e., $\gamma^{\mathrm{eff}} \to \gamma^{(1)}$ in sinuous mode.

A. Navier-Stokes cases without van der Waals forces at $N = 3$

When the surrounding fluids are inviscid $\mu_1 = \mu_3 = 0$, there is no $e^{l_i y}$ nor $e^{-l_i y}$ term for the velocity perturbation of the surrounding fluids and the velocity continuous on the interfaces is no

longer applicable. Thus, Eqs. (37) and (38) become

$$\begin{vmatrix} 1 & 1 & 1 \\ 0 & 2\mu_2 k^2 & \mu_2\left(k^2+l_2^2\right) \\ -\left(\rho_1\sigma_U^2+\gamma^{\text{eff}}k^3\right) & \left(\rho_2\sigma_U^2+2\mu_2k^2\sigma_U\right)\coth(kH_2/2) & 2\mu_2kl_2\sigma_U\coth(l_2H_2/2) \end{vmatrix}=0,$$

$$\Longrightarrow \mu_2\nu_2\left(k^2+l_2^2\right)^2\coth\left(\frac{kH_2}{2}\right)-4\mu_2\nu_2k^3l_2\coth\left(\frac{l_2H_2}{2}\right)+\rho_1\sigma_U^2+\gamma^{\text{eff}}k^3=0, \tag{39}$$

and

$$\begin{vmatrix} 1 & 1 & 1 \\ 0 & 2\mu_2 k^2 & \mu_2\left(k^2+l_2^2\right) \\ -\left(\rho_1\sigma_U^2+\gamma^{(1)}k^3\right) & \left(\rho_2\sigma_U^2+2\mu_2k^2\sigma_U\right)\tanh(kH_2/2) & 2\mu_2kl_2\sigma_U\tanh(l_2H_2/2) \end{vmatrix}=0,$$

$$\Longrightarrow \mu_2\nu_2(k^2+l_2^2)^2\tanh\left(\frac{kH_2}{2}\right)-4\mu_2\nu_2k^3l_2\tanh\left(\frac{l_2H_2}{2}\right)+\rho_1\sigma_U^2+\gamma^{(1)}k^3=0, \tag{40}$$

where $\nu_2=\mu_2/\rho_2$ is the kinematic viscosity. After neglecting the van der Waals interactions $\gamma^{\text{eff}}\to\gamma^{(1)}$, Eqs. (39) and (40) are identical with Li's results for viscous sheets moving in a gas [8]. When the sandwiched sheet is also inviscid $\mu_1=\mu_2=\mu_3=0$, the dispersion relations (39) and (40) can be further simplified into

$$\sigma_U^2\left[\rho_1+\rho_2\coth\left(\frac{kH_2}{2}\right)\right]+\gamma^{(1)}k^3=0, \tag{41}$$

and

$$\sigma_U^2\left[\rho_1+\rho_2\tanh\left(\frac{kH_2}{2}\right)\right]+\gamma^{(1)}k^3=0, \tag{42}$$

which are exactly the equations derived by Squire [6] for inviscid sheets.

B. Same surrounding fluids for Stokes problem at $N=3$

The dewetting instability of a viscous sheet sandwiched by another viscous fluid was studied by Liang [47] and Xu *et al.* [37]. Setting $\mu_1=\mu_3$, $\gamma^{(1)}=\gamma^{(2)}$ and solving the determinant equation (35) in the Stokes region, we can obtain one solution corresponding with their results:

$$\sigma=-\frac{\gamma^{\text{eff}}k}{2}\frac{\mu_2[\cosh(kH_2)-1]+\mu_1[\sinh(kH_2)-kH_2]}{\mu_2^2[\sinh(kH_2)+kH_2]+2\mu_1\mu_2\cosh(kH_2)+\mu_1^2[\sinh(kH_2)-kH_2]}, \tag{43}$$

where $\gamma^{\text{eff}}=\gamma^{(1)}-\frac{A_2}{k^2\pi H_2^4}$ is the effective interface tension including van der Waals forces. It is noted that the dispersion relation (43) corresponds to the varicose mode ($\varepsilon^{(1)}=-\varepsilon^{(2)}$). As mentioned above for the same surrounding fluids case at $N=3$ for the Navier-Stokes problem, the van der Waals interaction term in sinuous mode ($\varepsilon^{(1)}=\varepsilon^{(2)}$) for the Stokes problem would disappear. The dispersion relation in sinuous mode for the Stokes problem only has negative growth rate (not presented here), where the planar sheet is stabilized by the capillary forces.

IV. THREE-LAYER ($N=3$) CASE

In this section, we study the three-layer problem; a thin sheet (fluid 2) is sandwiched by fluid 1 and fluid 3. The surrounding fluids 1 and 3 could be either the same or different.

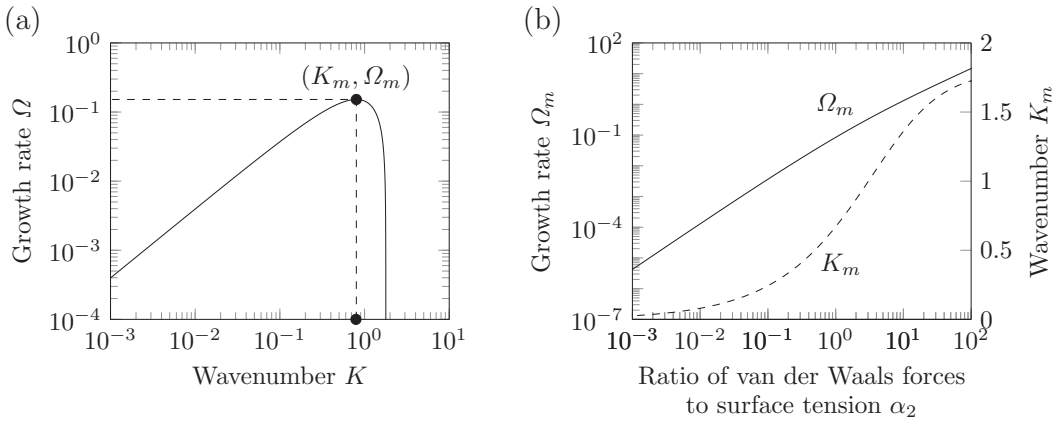

FIG. 2. $N = 3$ with the same surrounding fluids. (a) Growth rate Ω vs wave number K ($\alpha_2 = 1.6$, $\eta_1 = 1$). (b) Maximum growth rate Ω_m (solid line) and its corresponding wave number K_m (dashed line) dependent on dimensionless ratio α of van der Waals forces to interfacial tension ($\eta_1 = 1$).

A. The same surrounding fluids

When the surrounding fluids are the same $\eta_1 = \eta_3$, $\lambda^{(2)} = 1$, the dispersion relation (43) between the growth rate ω and the wave number k presented in Sec. III B can be nondimensionlized to

$$\Omega(K, \alpha_2, \eta_1) = \frac{2\alpha_2 - K^2}{2K} \times \frac{\eta_1(\sinh K - K) + (\cosh K - 1)}{\eta_1^2(\sinh K - K) + 2\eta_1 \cosh K + (\sinh K + K)}. \tag{44}$$

The growth rate Ω is associated with wave number K at $\alpha_2 = 1.6$, $\eta_1 = 1$ as seen in Fig. 2(a), and there is a maximum growth rate Ω_m with the most dangerous wave number K_m. As wave number $K \to 0$, from Eq. (44), the growth rate $\Omega(K, \alpha_2, \eta_1) \sim \alpha_2 K/(8\pi\eta_1) \to 0$. To further survey the effect of van der Waals forces, the maximum growth rate Ω_m and its corresponding wave number K_m as a function of α_2 at viscosity ratio $\eta_1 = 1$ is shown in Fig. 2(b). Growth rate Ω_m increases with α_2, and van der Waals forces become dominant and drive the dewetting instability [37].

Rather than the viscosity ratio $\eta_1 = 1$ in Fig. 2, the effect of this viscosity ratio η_1 on the maximum growth rate Ω_m at $\alpha_2 = 0.1$ is presented in Fig. 3. Obviously, the increasing viscosity

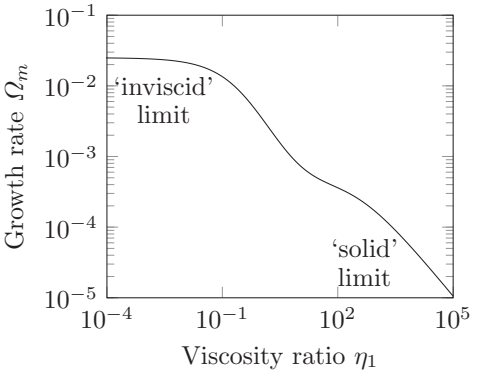

FIG. 3. $N = 3$ with the same surrounding fluids: maximum growth rate Ω_m vs the viscosity ratio η_1 at $\alpha_2 = 0.1$.

ratio η_1 decreases the growth rate Ω_m, as a stabilizing factor. When the viscosity ratio $\eta_1 \ll 1$,

$$\Omega = \frac{2\alpha_2 - K^2}{2K} \times \frac{(\cosh K - 1)}{(\sinh K + K)} \quad \text{at } \eta_1 \to 0$$

with a maximum limit of growth rate $\Omega_m \to 0.025$, i.e., the surrounding fluids 1 and 3 become inviscid (the "inviscid" limit). On the other hand, when the viscosity ratio $\eta_1 \gg 1$,

$$\Omega = \frac{2\alpha_2 - K^2}{2K} \times \frac{1}{\eta_1} \quad \text{at } \eta_1 \to \infty,$$

with the growth rate decreasing as η_1 increases ($\Omega \sim 1/\eta_1$) and then the liquid sheet would be stable when the viscosity of surrounding fluids is infinitely large (the "solid" limit).

B. Different surrounding fluids

For this case, it could be different viscosity ($\eta_1 \neq \eta_3, \lambda^{(2)} = 1$), different interface tension ($\eta_1 = \eta_3, \lambda^{(2)} \neq 1$), or different viscosity and interface tension ($\eta_1 \neq \eta_3, \lambda^{(2)} \neq 1$). In addition, compared to the same surrounding fluids case, the eigenamplitudes of two solutions would no longer be $\varepsilon^{(1)} = \varepsilon^{(2)}$ (sinuous) and $\varepsilon^{(1)} = -\varepsilon^{(2)}$ (varicose) where the absolute values of amplitudes are different. Following Li's work [16], one solution is called the "para-sinuous" mode (when phase difference between two interfaces is close to zero, $\varepsilon^{(1)}\varepsilon^{(2)} > 0$) and the other is the "para-varicose" mode (when phase difference between two interfaces is close to π, $\varepsilon^{(1)}\varepsilon^{(2)} < 0$). For the dewetting instability, the destabilizing van der Waals forces are proportional to the thickness perturbation $\tilde{H} = \varepsilon^{(1)} - \varepsilon^{(2)}$. From numerical calculations, it is found there are also two solutions: one positive growth rate ω corresponding to the para-varicose mode with larger thickness perturbations, and the other negative ω corresponding to the para-sinuous mode. In the para-sinuous mode, the calculated eigenamplitudes $\varepsilon^{(1)} \approx \varepsilon^{(2)}$, and then the thickness perturbation $\tilde{H} = \varepsilon^{(1)} - \varepsilon^{(2)}$ is very small. The capillary forces still dominate and stabilize the planar sheets in the para-sinuous mode. Thus, only the solution with a positive growth rate in para-varicose mode will be presented in this subsection.

1. Different viscosity but the same interfacial tension ($\eta_1 \neq \eta_3, \lambda^{(2)} = 1$)

Figure 4(a) shows the growth rates Ω versus the wave number K for several pairs of viscosity ratio η_1 and η_3 ($\alpha_2 = 0.1$). It is clear that larger viscosity ratio (η_2 or η_3) decreases the growth rate and the unstable wave-number range. Further, the dependence of the maximum growth rate Ω_m on the viscosity ratio η_3 while the other viscosity ratio is fixed at $\eta_1 = 1$ and 10 ($\alpha_2 = 0.1$) is presented in Fig. 4(b). Again, the increasing viscosity ratio η_3 destabilizes the sheets with a smaller growth rate Ω_m. The eigenamplitude ratio $\chi = \varepsilon^{(1)}/\varepsilon^{(2)}$ in para-varicose mode at $\eta_1 = 1, \eta_3 = 10$ is shown in Fig. 4(c), and the eigenamplitude ratio χ_m corresponds to the maximum growth rate (K_m, Ω_m). The dashed line in Fig. 4(c) is the eigenamplitude ratio for the same surrounding fluids ($\eta_1 = \eta_3 = 1$ and 10), recovering the dominance of varicose mode for the same surrounding fluids case. To study the effect of viscosity ratio, the eigenamplitude ratio χ_m versus the ratio η_3 is plotted in Fig. 4(d). The eigenamplitude ratio χ_m becomes larger as the viscosity ratio η_3 increases.

It is noted, compared to the same surrounding fluids case in Fig. 2, that the growth rate Ω_m reaches the minimum at $\eta_3 \to \infty$ (solid limit) besides the maximum value at $\eta_3 \to 0$ (inviscid limit). When the viscosity of fluid 3 is very high, $\eta_3 \gg 1$, the eigenamplitude ratio $\chi_m \to \infty$, denoting that there is almost no perturbation at interface 2 (between fluid 2 and fluid 3) compared to the perturbations at interface 1 (between fluid 1 and fluid 2). At this limit region, perturbations only appear at the interface between fluids 1 and 2, where the extremely viscous fluid 3 can be assumed as a solid media (called the solid limit). At the inviscid limit $\eta_3 \ll 1$, the eigenamplitude ratio χ_m reaches a limit, where the thin sheet 2 seems sandwiched by the fluid 1 and an inviscid gas. For both solid limit $\eta_3 \gg 1$ and inviscid limit $\eta_3 \ll 1$, the growth rate and corresponding eigenamplitudes are determined by the other surrounding fluid viscosity η_1.

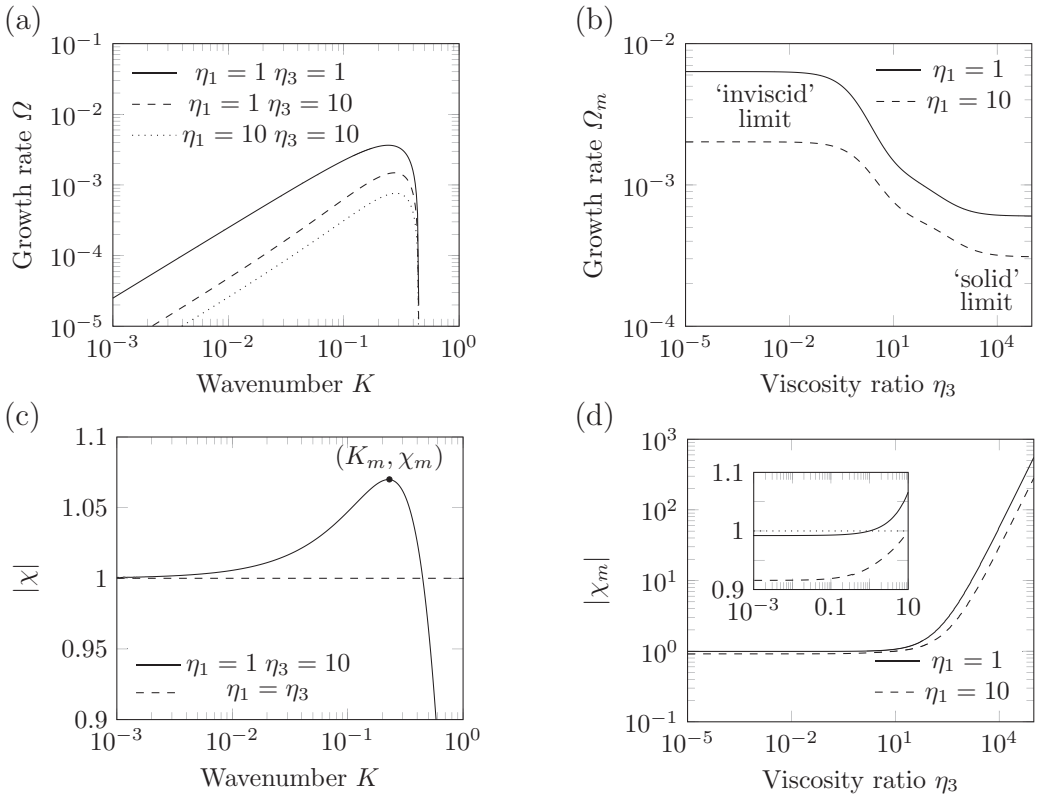

FIG. 4. $N = 3$ with surrounding fluids of different viscosity ($\eta_1 \neq \eta_3$, $\lambda^{(2)} = 1$, $\alpha_2 = 0.1$). (a) Growth rate Ω vs wave number K at several pairs of viscosity ratio η_1 and η_3. (b) Maximum growth rate Ω_m dependent on the viscosity ratio η_3 at different viscosity ratio $\eta_1 = 1$ and $\eta_1 = 10$. (c) Eigenamplitude ratio χ as a function of wave number K at $\eta_1 = 1$, $\eta_3 = 10$ (solid line) and $\eta_1 = \eta_3$ (dashed line). (d) Eigenamplitude ratio χ_m corresponding to maximum growth rate Ω_m in Fig. 4(b), and the inset for the zoom-in view for $10^{-3} < \eta_3 < 10$.

2. The same viscosity but different interfacial tension ($\eta_1 = \eta_3$, $\lambda^{(2)} \neq 1$)

Let us consider the case where the surrounding viscosities $\eta_1 = \eta_3$ but the interfacial tension of two interfaces $\gamma^{(1)} \neq \gamma^{(2)}$ (i.e. $\lambda^{(2)} \neq 1$). As shown in Fig. 5(a), the growth rate Ω_m decreases as the interfacial tension ratio $\lambda^{(2)}$ increases, suggesting again the interfacial tension as a stabilizing factor. The eigenamplitude ratios χ_m corresponding to the maximum growth rate Ω_m at different interfacial tension ratios $\lambda^{(2)}$ are presented in Fig. 5(b). Obviously, a larger interfacial tension ratio $\lambda^{(2)}$ yields a larger eigenamplitude ratio $|\chi_m|$.

The more general case $\eta_1 \neq \eta_3$, $\lambda^{(2)} \neq 1$ is the combination of the above cases $\eta_1 \neq \eta_3$, $\lambda^{(2)} = 1$ and $\eta_1 = \eta_3$, $\lambda^{(2)} \neq 1$, where the effects of the viscosity and interfacial tension on the instability and eigenamplitude are similar to the conclusions in Secs. IV B 1 and IV B 2.

V. FOUR-LAYER ($N = 4$) CASE

A. Two unstable modes

For the four-layer problem $N = 4$, an extra layer liquid sheet inside (third layer, i.e., the cladding layer) and the associated interface make the instability analysis more complicated. The simplest case with $\eta_3 = 1$, $\lambda^{(2)} = \lambda^{(3)} = 1$, $H_3/H_2 = 1$, $\alpha_2 = \alpha_3 = 0.1$ (the properties of cladding fluid 3 corresponding with thin liquid sheet 2) is taken as the reference case. In Fig. 6(a), the growth rate

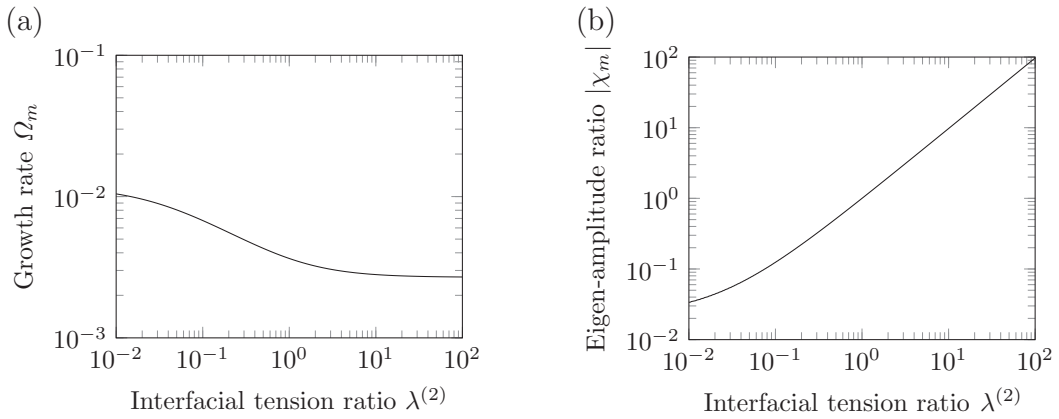

FIG. 5. $N = 3$ with surrounding fluids of different interfacial tension ($\eta_1 = \eta_3, \lambda^{(2)} \neq 1, \alpha_2 = 0.1$). (a) Maximum growth rate Ω_m dependent on the interfacial tension ratio $\lambda^{(2)}$. (b) Eigenamplitude ratio χ_m corresponding to maximum growth rate Ω_m in Fig. 5(a).

Ω versus wave number K of this reference case at surrounding fluids viscosities $\eta_1 = \eta_4 = 10$ is plotted. In contrast to the three-layer problem, there are two positive solutions of growth rate Ω, and solution 1 and 2 are, respectively, indicated by the dark and gray line in Fig. 6(a). At smaller wave number $K < K_t$, the solution 1 is larger; but at larger wave number $K > K_t$ the other solution 2 becomes larger than the solution 1. The eigenamplitudes corresponding to the larger growth rate [the solid line in Fig. 6(a)] are shown in Fig. 6(b).

For the solution 1, the eigenamplitudes ($\varepsilon^{(1)} = -\varepsilon^{(3)}$, $\varepsilon^{(2)} \approx 0$) imply that the perturbation amplitude at the second interface is negligible, and then layer 2 and layer 3 can be treated as a new integrated layer. As the amplitudes at the first and third interface are opposite, the para-varicose mode is for this new integrated layer (mode A). For the solution 2, the eigenamplitudes ($\varepsilon^{(1)} = \varepsilon^{(3)} \approx -0.4$, $\varepsilon^{(2)} \approx 0.8$), the para-varicose mode is for both second and third layer thin sheets (mode B). As wave number K increases to larger than K_t in this case, the dominating mode changes from mode A to mode B.

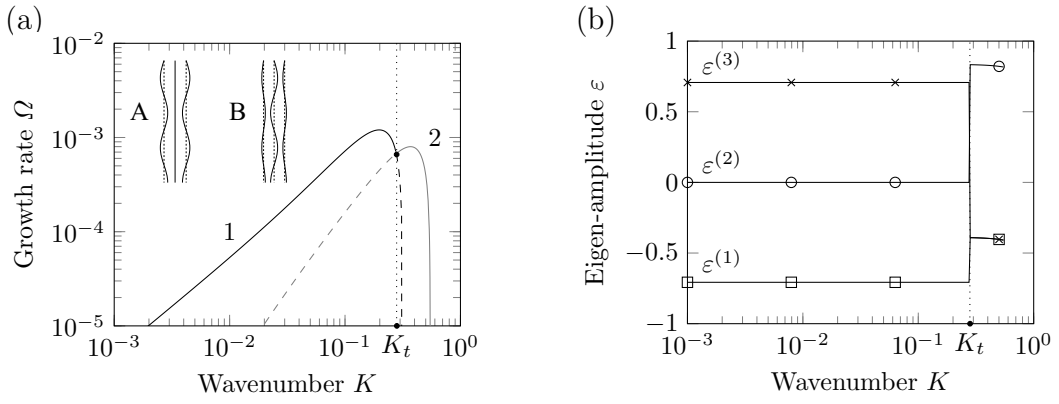

FIG. 6. $N = 4$ four-layer reference case at $\eta_3 = 1, \lambda^{(2)} = \lambda^{(3)} = 1, H_3/H_2 = 1, \alpha_2 = \alpha_3 = 0.1$ and surrounding fluids $\eta_1 = \eta_4 = 10$. (a) Growth rate Ω vs wave number K. (b) Eigenamplitudes $\boldsymbol{\varepsilon}$ corresponding to growth rate Ω in Fig. 6(a). With increasing wave number K, the dominating mode changes from mode A to mode B.

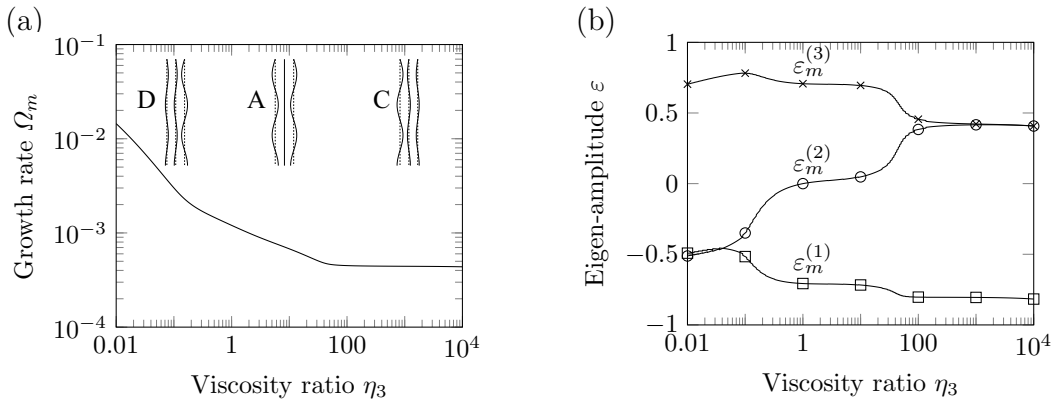

FIG. 7. Different cladding layer viscosities η_3 for the four-layer ($N = 4$) problem at $\lambda^{(2)} = \lambda^{(3)} = 1, H_3/H_2 = 1, \alpha_2 = \alpha_3 = 0.1$ and surrounding fluids $\eta_1 = \eta_4 = 10$: (a) maximum growth rates Ω_m and (b) their corresponding eigenamplitudes $\boldsymbol{\varepsilon}_m$. For $\eta_3 < 0.1$, "mode D" with eigenamplitudes $\varepsilon_m^{(1)} \approx \varepsilon_m^{(2)} \approx -0.5,\ \varepsilon_m^{(3)} \approx 0.75$ dominates the instability; for $0.1 < \eta_3 < 20$, mode A with $\varepsilon_m^{(1)} \approx -\varepsilon_m^{(3)},\ \varepsilon_m^{(2)} \approx 0$ dominates; for $\eta_3 > 100$, mode C with $\varepsilon_m^{(1)} \approx -0.8,\ \varepsilon_m^{(2)} = \varepsilon_m^{(3)} \approx 0.4$ dominates.

B. The effect of third layer viscosity

To study the effect of the cladding layer viscosity (third layer) η_3 on the instability, the maximum growth rate Ω_m as a function of the viscosity ratio η_3 at $\eta_1 = \eta_4 = 10, \alpha_2 = \alpha_3 = 0.1, \lambda^{(2)} = \lambda^{(3)} = 1, H_3/H_2 = 1$ is presented in Fig. 7(a). Meanwhile, the eigenamplitudes $\varepsilon_m^{(1)}$, $\varepsilon_m^{(2)}$, and $\varepsilon_m^{(3)}$ corresponding to the maximum growth rate Ω_m are shown in Fig. 7(b).

When fluid 3 is much more viscous than fluid 2 $\eta_3 > 100$, the growth rate Ω_m is nearly independent on η_3, and its eigenamplitudes $\varepsilon_m^{(1)} \approx -0.8,\ \varepsilon_m^{(2)} = \varepsilon_m^{(3)} \approx 0.4$ (the para-varicose mode on the second layer sheet, mode C). At $0.1 < \eta_3 < 20$, the maximum growth rate Ω_m decreases as the viscosity ratio η_3 increases and the corresponding eigenamplitudes $\varepsilon_m^{(1)} \approx -\varepsilon_m^{(3)},\ \varepsilon_m^{(2)} \approx 0$, i.e., mode A dominates the instability.

When fluid 3 is much less viscous $\eta_3 < 0.1$, the increasing viscosity ratio η_3 also decreases the maximum growth rate Ω_m but more quickly than $0.1 < \eta_3 < 20$. Here at $\eta_3 < 0.1$, the eigenamplitudes $\varepsilon_m^{(1)} \approx \varepsilon_m^{(2)} \approx -0.5,\ \varepsilon_m^{(3)} \approx 0.75$, i.e., the para-varicose mode on the third layer sheet dominates (mode D).

Thus, at $\eta_3 > 100$ or $\eta_3 < 0.1$, the instability is dominated by the para-varicose mode on the less viscous thin sheet: at $\eta_3 > 100$, the para-varicose mode on the second layer sheet, the growth rate Ω_m almost does not change as third layer viscosity η_3 further increases (viscosity of the second sheet fixed here); at $\eta_3 < 0.1$, the para-varicose mode on the third layer sheet, the growth rate Ω_m increases as the viscosity ratio η_3 decreases.

C. The effect of interfacial tension

To investigate the effect of interfacial tension $\gamma^{(2)}$ on the interface between the second layer and the third layer, the maximum growth rate Ω_m as a function of the interfacial tension ratio $\lambda^{(2)} = \gamma^{(2)}/\gamma^{(1)}$ between first and second interfaces and their corresponding eigenamplitudes $\varepsilon_m^{(1)}, \varepsilon_m^{(2)}, \varepsilon_m^{(3)}$ are presented in Figs. 8(a) and 8(b) ($\eta_1 = \eta_4 = 10, \eta_3 = 1, \alpha_2 = \alpha_3 = 0.1, \lambda^{(3)} = 1, H_3/H_2 = 1$). When the interfacial tension $\gamma^{(2)}$ is smaller than $\gamma^{(1)}$ and $\gamma^{(3)}$, i.e., $\lambda^{(2)} < 0.05$, the increasing interfacial tension ration $\lambda^{(2)}$ stabilizes the sheets with smaller growth rate Ω_m and the eigenamplitudes $\varepsilon_m^{(1)} = \varepsilon_m^{(3)} < 0,\ \varepsilon_m^{(2)} \to 1$ (mode E). At $\lambda^{(2)} > 1$, the growth rate Ω_m rarely varies as interfacial tension ratio $\lambda^{(2)}$ increases and the dominating mode changes to mode A ($\varepsilon_m^{(1)} = -\varepsilon_m^{(3)},\ \varepsilon_m^{(2)} \approx 0$).

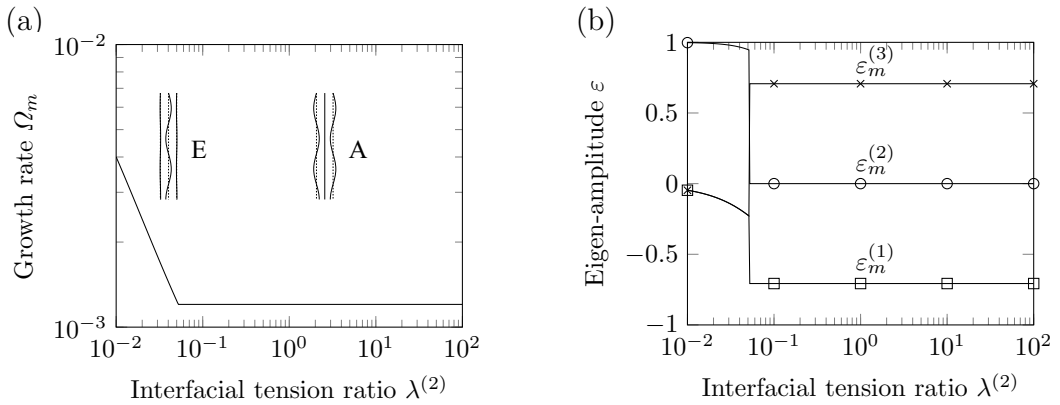

FIG. 8. Different interfacial tension $\lambda^{(2)}$ for the four-layer ($N = 4$) problem at $\eta_3 = 1, \lambda^{(3)} = 1, H_3/H_2 = 1, \alpha_2 = \alpha_3 = 0.1$ and surrounding fluids $\eta_1 = \eta_4 = 10$: (a) maximum growth rates Ω_m and (b) their corresponding eigenamplitudes $\boldsymbol{\varepsilon}_m$. For $\lambda^{(2)} < 0.05$, mode E with eigenamplitudes $\varepsilon_m^{(1)} = \varepsilon_m^{(3)} < 0$, $\varepsilon_m^{(2)} \to 1$ dominates; for $\lambda^{(2)} > 1$, mode A with $\varepsilon_m^{(1)} = -\varepsilon_m^{(3)}$, $\varepsilon_m^{(2)} \approx 0$ dominates.

D. The effect of layer thickness

Now let us focus on the effect of the cladding layer thickness H_3 on the dewetting instability, the maximum growth rate Ω_m versus thickness ratio H_3/H_2 at $\eta_1 = \eta_4 = 10, \eta_3 = 1, \lambda^{(2)} = \lambda^{(3)} = 1, \alpha_2 = 0.1, \alpha_3|_{H_3/H_2=1} = 0.1$ shown in Fig. 9(a). When the thickness ratio H_3/H_2 is large enough, van der Waals forces due to the cladding layer H_3 can be neglected (i.e., $\alpha_2 \gg \alpha_3$ and $\alpha_3 \ll 1$). The growth rate Ω_m approaches the value $\Omega_{m,N=3}$ of the three-layer problem where the thin sheet of fluid 2 with thickness H_2 is sandwiched by the surrounding fluid 1 and the thick layer sheet of fluid 3 in Fig. 9(a) and the dominating eigenamplitudes also switch to the para-varicose mode for a three-layer problem (mode F, $\varepsilon_m^{(1)} = -\varepsilon_m^{(2)}, \varepsilon_m^{(3)} \approx 0$) in Fig. 9(b). Thus, when the cladding

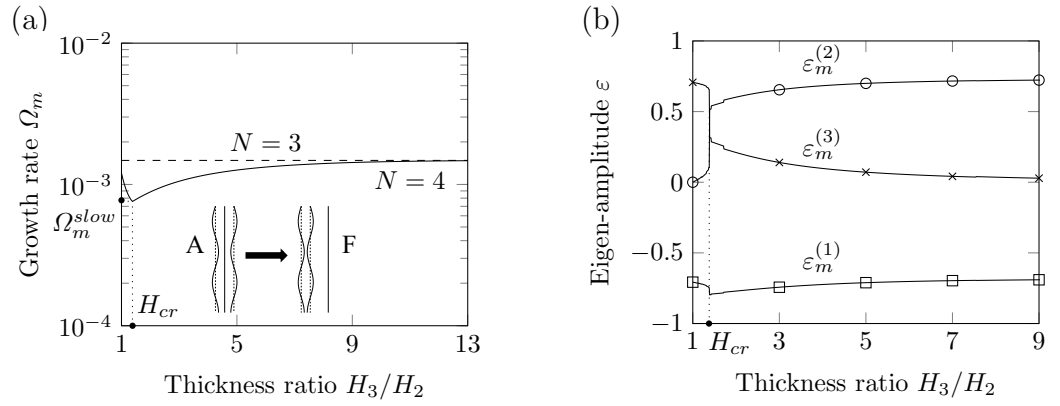

FIG. 9. Different cladding layer thicknesses H_3/H_2 for the four-layer ($N = 4$) problem at $\eta_3 = 1, \lambda^{(2)} = \lambda^{(3)} = 1, \alpha_2 = 0.1, \alpha_3|_{H_3/H_2=1} = 0.1$ and surrounding fluids $\eta_1 = \eta_4 = 10$. (a) Maximum growth rates Ω_m (solid line), the three-layer limit ($N = 3, \eta_1 = 10, \eta_3 = 1$, dashed line), and the slowest growth rate Ω_m^{slow} associated with a critical thickness H_{cr}. (b) The eigenamplitudes $\boldsymbol{\varepsilon}_m$ corresponding to Ω_m. With $H_3 \sim H_2$, mode A dominates and the growth rate Ω_m is smaller at larger cladding layer thickness H_3; with large enough H_3/H_2, mode F dominates where van der Waals forces due to the cladding layer H_3 can be neglected and the growth rate Ω_m slowly increases to the limit value $\Omega_{m,N=3}$ as the thickness H_3 increases.

TABLE I. Controlling instability or the perturbation growth rates through designing various structures for application of fiber drawing (Hamaker constant of thin sheets $A_j \sim 10^{-17}$ J, interfacial tension of interfaces $\gamma^{(i)} \sim 10^{-1}$ N m^{-1}).

Structure	Viscosities (Pa s)	Thicknesses (nm)	Growth rate ω_m (s^{-1})
PES/As_2Se_3/PES	$10^5/10^5/10^5$	$\infty/10/\infty$	0.703
PSU/Se/PSU	$10^5/1/10^5$	$\infty/80/\infty$	0.184
PES/As_2Se_3/PES	$10^5/10^5/10^5$	$\infty/50/\infty$	1.33×10^{-3}
PES/As_2Se_3/Se	$10^5/10^5/1$	$\infty/50/\infty$	2.56×10^{-3}
PES/As_2Se_3/Se/PES	$10^5/10^5/1/10^5$	$\infty/50/50/\infty$	0.952
PSU/Se/As_2Se_3/PSU	$10^5/1/10^5/10^5$	$\infty/30/30/\infty$	5.557
PSU/Se/As_2Se_3/PSU	$10^5/1/10^5/10^5$	$\infty/30H_{cr}/30/\infty$	0.0191
Se/As_2Se_3/PSU	$1/10^5/10^5$	$\infty/30/\infty$	0.0191

layer is thick, the $N = 4$ four-layer problem can be simplified to a three-layer problem. Under this para-varicose mode for a three-layer problem with large H_3, the growth rate Ω_m slowly increases to the limit value $\Omega_{m,N=3}$ as the thickness H_3 increases.

In contrast, under the instability mode for a four-layer problem with thickness $H_3 \sim H_2$ [here mode A in Fig. 9(b)], the growth rate Ω_m is smaller at larger cladding layer thickness H_3. Thus, there is a critical thickness of the cladding layer H_{cr} to yield the slow growth rate Ω_m^{slow}, as shown in Fig. 9(a). Similar results about the effect of the cladding layer thickness H_3 at other parameters, such as $\eta_3 \neq 1$ or $\lambda^{(2)} \neq 1$, can be obtained.

VI. APPLICATIONS OF FIBER DRAWING

Three-layer $N = 3$ and four-layer $N = 4$ structures are carefully studied as above, and these results could provide guidance to design and fabricate more sophisticated functional micro/nanodevices in fibers and textiles via thermal drawing [23]. Besides material selection of various viscosity and interfacial tension [26,28,29], here we focus on the design of composite structure to manipulate this dewetting instability through multilayers and their thicknesses, as studied in Sec. V and listed in Table I.

First, for $N = 3$ and the same surrounding viscosity, the inner sheet with higher viscosity should be thinner so that larger van der Waals forces promote the instability of the thin sheet. For example, listed in Table I are growth rates for the 10-nm As_2Se_3 sheet in the PES/As_2Se_3/PES structure ($\alpha_2 = 0.1$) and for the 80-nm Se sheet in the PSU/Se/PSU structure ($\alpha_2 = 0.0016$). Indeed, as mentioned in the introduction for filamentation instability [28], in the PES/As_2Se_3/PES structure, the thickness of the As_2Se_3 sheet should be drawn to less than 10 nm, and in the PSU/Se/PSU structure Se sheet thickness should be less than 100 nm.

Second, the instability or the perturbation growth rate can be promoted or increased for high viscous materials, resulting in filamentation of the thin sheet. For example, for the $N = 3$ PES/As_2Se_3/PES structure, $\omega_m = 1.33 \times 10^{-3}$ s^{-1} for the 50-nm As_2Se_3 sheet in Table I. An additional Se layer can enhance the instability growth rate $\omega_m = 0.952$ s^{-1} by nearly *three orders of magnitude*, i.e., a $N = 4$ PES/As_2Se_3/Se/PES structure with $H_{As_2Se_3} = H_{Se} = 50$ nm, as shown in Table I (growth rate much larger than the one in the PES/As_2Se_3/Se structure with a less viscous surrounding fluid).

Physically, although less viscous fluid could be used as the surrounding fluids to enhance the instability, but there is an upper limit of the growth rate (the inviscid limit) by decreasing the surrounding fluid viscosity according to Figs. 3 and 4(b). It is noted that for $N = 4$ and $H_3 \approx H_2$ the instability will be dominated by the much less viscous thin sheet, and the growth rate increases as the viscosity of the cladding layer decreases [Fig. 7(a)]. Clearly, the growth rate $\Omega_m \approx 0.015$ in

Fig. 7(a) with cladding layer viscosity $\eta_3 = 0.01$ at $H_3 \approx H_2$ and $N = 4$ is larger than corresponding growth rates at $N = 3$ with $\eta_1 = \eta_3 = 0.01$ in Fig. 3(a) and $\eta_3 = 0.01$ in Fig. 4(b). Thus, a cladding layer of less viscous fluid with thickness $H_3 \approx H_2$ is better than directly using this less viscous fluid as a surrounding fluid.

Third, the instability or the perturbation growth rate can be suppressed or reduced for the less viscous material, preserving the thin sheet or uniform layer structure in the produced fiber. For example, for the $N = 4$ PSU/Se/As_2Se_3/PSU structure with $H_{As_2Se_3} = H_{Se} = 30$ nm ($\omega_m = 5.557\,s^{-1}$) in Table I, although the high viscous As_2Se_3 layer slightly reduces the perturbation growth rate, the dewetting instability should be dominated by the less viscous Se layer. To further suppress the dewetting instability, the thickness of the less Se viscous layer could be increased to $H_{Se} = H_{cr} \times 30$ nm to obtain a slow growth rate Ω_m^{slow}, where the dominating instability mode would switch to the para-varicose mode for three-layer problem of the high viscous As_2Se_3 layer with a much smaller perturbation growth rate in Table I. Here $H_{cr} \approx 4.4$, and growth rate decreases to $\omega_m = 0.0191\,s^{-1}$ (nearly the same as its corresponding three-layer case) by around *two orders of magnitude*. This makes possible the fabrication of a long fiber including less viscous material with smaller diameter.

It is noteworthy that in the above analysis for applications of fiber drawing the stretching effect is not considered. The total growth of perturbations and breakup results during the thermal drawing process can be obtained by combining the stretching [37,38]. Moreover, nonlinear evolution could be incorporated to describe the breakup of a stretching sheet. But the linear analysis here is still informative and helpful for the preform design in fiber drawing to enhance or suppress the instability.

Similar analysis can be expanded to the system with more layers. Especially, a certain thick layer with its ratio of van der Waals forces to interfacial tension $\alpha_c \ll 1$ can be considered as the surrounding fluid for the nearby thin layers. Thus, thick sheet layers can be used as separate layers to reduce the crosstalk or interference effect between the neighbor layers, and the multilayer system can be divided to several three-layer, four-layer, or five-layer subproblems to achieve highly integrated in-fiber composite nanostructures during one thermal-drawing process [28].

VII. DISCUSSIONS AND CONCLUSIONS

More future work can be explored from several aspects.

(1) The Stokes problems are solved in Secs. IV and V, but inertial contributions (including the time derivative term) to the dewetting instability could be included. A suitable numerical iteration method should be chosen to solve the nonlinear eigenvalue problem.

(2) Only long-range interactions with the two nearest interfaces for each interface are considered in this paper, since the perturbations of van der Waals forces are proportional to $1/H^4$. The interactions besides the two nearest interfaces can be considered in the analysis to be more accurate.

(3) The non-Newtonian behaviors of the molten materials (such as the viscoelasticity, the shear thinning or thickening viscosity, or the dependence of viscosity on the temperature), thermal fluctuations, and spontaneous nucleation can be incorporated into the analysis.

(4) Despite the excellent prediction of the onset instability by the linear analysis, the nonlinear evolution and stretching effect following the total growth rate method in Javadi *et al.* [38] and Xu *et al.* [37] can be combined in the linear instability analysis, to better study the instability and breakup in the thermal drawing process.

(5) More complicated geometries could be considered, such as hierarchical textures on the cross section instead of simple parallel structure [25].

In summary, the linear analysis of dewetting instability is performed for multilayer planar sheets for various physical parameters, including van der Waals forces, thicknesses, viscosities, and surface tensions. For the three-layer case, the dewetting instability due to van der Waals forces is dominated by the para-varicose mode with larger thickness perturbations, in contrast with a planar liquid sheet moving in a gas where the aerodynamic force dominates the instability and the para-sinuous mode is more unstable. For the four-layer case, there are several more complicated unstable modes,

and the maximum growth rate (Ω_m) depends on both fluid properties, and the corresponding eigenamplitudes can switch among various modes. Particularly, a slowest growth rate (Ω_m^{slow}) is identified at a critical thickness of the cladding layer (H_{cr}). Additionally, for relevant applications of fiber drawing, by changing multilayer structure from $N = 3$ to 4 through introducing an additional less viscous sheet, the instability can be enhanced, or, by choosing a suitable thickness of a less viscous sheet, the instability can be reduced.

These results not only shed light on controlling the dewetting instability by material selection and structure designing, but also provide guidance to achieve functional devices with sophisticated nanostructures either in a single fiber or in integrated fabrics for large-scale textiles. Our paper might be also helpful for the multilayer coextrusion process in polymer film production [48–52], where instability could lead to unexpected holes or breakup altering final properties [53–56] when the layer thickness is reduced down to nanometer scale. Zhu *et al.* [57] investigated the hole evolution and breakup in the dewetting instability by nucleation during multilayer coextrusion based on Krausch's [58] and Wang *et al.*'s [59] work, and pointed out that the dynamics of hole formation is unaffected by the originating mechanism of film rupture (nucleation or spinodal dewetting). Our paper for multilayer liquid sheets could not only predict the onset of spinodal dewetting instability driven by van der Waals forces, but also provide possible methods to suppress this instability during multilayer coextrusion.

ACKNOWLEDGMENTS

This work was supported by the National Program in China and startup from Fudan University, and the China Postdoctoral Science Foundation.

[1] A. Oron, S. H. Davis, and S. G. Bankoff, Long-scale evolution of thin liquid films, Rev. Mod. Phys. **69**, 931 (1997).
[2] R. V. Craster and O. K. Matar, Dynamics and stability of thin liquid films, Rev. Mod. Phys. **81**, 1131 (2009).
[3] F. Gallaire and P.-T. Brun, Fluid dynamic instabilities: Theory and application to pattern forming in complex media, Phil. Trans. R. Soc. A **375**, 20160155 (2017).
[4] R. G. Dorman, The atomization of liquid in a flat spray, Br. J. Appl. Phys. **3**, 189 (1952).
[5] N. Dombrowski and R. P. Fraser, A photographic investigation into the disintegration of liquid sheets, Phil. Trans. R. Soc. A **247**, 101 (1954).
[6] H. B. Squire, Investigation of instability of a moving liquid film, Br. J. Appl. Phys. **4**, 167 (1953).
[7] W. W. Hagerty and J. F. Shea, A study of the stability of plane fluid sheets, J. Appl. Mech. **22**, 509 (1955).
[8] X. Li and R. S. Tankin, On the temporal instability of a two-dimensional viscous liquid sheet, J. Fluid Mech. **226**, 425 (1991).
[9] R. H. Rangel and W. A. Sirignano, The linear and nonlinear shear instability of a fluid sheet The linear and nonlinear shear instability of a fluid sheet, Phys. Fluids **3**, 2392 (1991).
[10] D. R. Brown, A study of the behaviour of a thin sheet of moving liquid, J. Fluid Mech. **10**, 297 (1961).
[11] S. P. Lin, Stability of a viscous liquid curtain, J. Fluid Mech. **104**, 111 (1981).
[12] S. P. Lin, Z. W. Lian, and B. J. Creighton, Absolute and convective instability of a liquid sheet, J. Fluid Mech. **220**, 673 (1990).
[13] E. A. Ibrahim and E. T. Akpan, Three-dimensional instability of viscous liquid sheets, Atomization and Sprays **6**, 649 (1996).
[14] Z. Liu, G. Brenn, and F. Durst, Linear analysis of the instability of two-dimensional non-Newtonian liquid sheets, J. Non-Newtonian Fluid Mech. **78**, 133 (1998).
[15] G. Brenn, Z. Liu, and F. Durst, Three-dimensional temporal instability of non-Newtonian liquid sheets, Atomization and Sprays **11**, 49 (2001).

[16] X. Li, On the instability of plane liquid sheets in two gas streams of unequal velocities, Acta Mechanica **106**, 137 (1994).
[17] L. Yang, B. Xu, and Q. Fu, Linear instability analysis of planar non-Newtonian liquid sheets in two gas streams of unequal velocities, J. Non-Newtonian Fluid Mech. **167-168**, 50 (2012).
[18] R. J. Dyson, J. Brander, C. J. W. Breward, and P. D. Howell, Long-wavelength stability of an unsupported multilayer liquid film falling under gravity, J. Eng. Math. **64**, 237 (2009).
[19] H. Ye, L. Yang, and Q. Fu, Spatial instability of viscous double- layer liquid sheets, Phys. Fluids **28**, 102101 (2016).
[20] S. D. Hart, G. R. Maskaly, B. Temelkuran, P. H. Prideaux, J. D. Joannopoulos, and Y. Fink, External Reflection from Omnidirectional Dielectric Mirror Fibers, Science **296**, 510 (2002).
[21] K. Kuriki, O. Shapira, S. D. Hart, G. Benoit, Y. Kuriki, J. F. Viens, M. Bayindir, J. D. Joannopoulos, and Y. Fink, Hollow multilayer photonic bandgap fibers for NIR applications, Opt. Express **12**, 1510 (2004).
[22] E. Pone, C. Dubois, N. Guo, Y. Gao, A. Dupuis, F. Boismenu, S. Lacroix, and M. Skorobogatiy, Drawing of the hollow all-polymer Bragg fibers, Opt. Express **14**, 5838 (2006).
[23] A. F. Abouraddy, M. Bayindir, G. J. Benoit, S. D. Hart, K. Kuriki, N. D. Orf, O. Shapira, F. Sorin, B. Temelkuran, and Y. Fink, Towards multimaterial multifunctional fibres that see, hear, sense and communicate, Nat. Mater. **6**, 336 (2007).
[24] F. Sorin, A. F. Abouraddy, N. Orf, O. Shapira, J. Viens, J. Arnold, J. D. Joannopoulos, and Y. Fink, Multimaterial photodetecting fibers: A geometric and structural study, Adv. Mater. **19**, 3872 (2007).
[25] T. Nguyendang, A. C. de Luca, W. Yan, Y. Qu, A. G. Page, M. Volpi, T. D. Gupta, S. P. Lacour, and F. Sorin, Controlled sub-micrometer hierarchical textures engineered in polymeric fibers and microchannels via thermal drawing, Adv. Functional Mater. **27**, 1605935 (2017).
[26] D. Deng, J. C. Nave, X. Liang, S. G. Johnson, and Y. Fink, Exploration of in-fiber nanostructures from capillary instability, Opt. Express **19**, 16273 (2011).
[27] X. Liang, D. Deng, J. C. Nave, and S. G. Johnson, Linear stability analysis of capillary instabilities for concentric cylindrical shells, J. Fluid Mech. **683**, 235 (2011).
[28] D. Deng, N. D. Orf, A. F. Abouraddy, A. M. Stolyarov, J. D. Joannopoulos, H. A. Stone, and Y. Fink, In-fiber semiconductor filament arrays, Nano Lett. **8**, 4265 (2008).
[29] B. Xu, S. Ma, Y. Xiang, J. Zhang, M. Zhu, L. Wei, G. Tao, and D. Deng, In-fiber structured particles and filament arrays from the perspective of fluid instabilities, Advanced Fiber Materials **2**, 1 (2020).
[30] P.-G. de Gennes, F. Brochard-wyart, and D. Quere, *Capillarity and Wetting Phenomena* (Springer, New York, 2004).
[31] G. Reiter, Dewetting of Thin Polymer Films, Phys. Rev. Lett. **68**, 75 (1992).
[32] G. Reiter, Unstable thin polymer films: Rupture and dewetting processes, Langmuir **9**, 1344 (1993).
[33] F. Brochard-Wyart, P.-G. de Gennes, H. Hervert, and C. Redon, Wetting and slippage of polymer melts on semi-ideal surfaces, Langmuir **10**, 1566 (1994).
[34] A. Sharma and R. Khanna, Pattern Formation in Unstable Thin Liquid Films, Phys. Rev. Lett. **81**, 3463 (1998).
[35] G. Reiter, A. Sharma, A. Casoli, M. O. David, R. Khanna, and P. Auroy, Thin film instability induced by long-range forces, Langmuir **15**, 2551 (1999).
[36] F. Brochard-Wyart, P. Martin, and C. Redon, Liquid/liquid dewetting, Langmuir **9**, 3682 (1993).
[37] B. Xu, M. Li, F. Wang, S. G. Johnson, Y. Fink, and D. Deng, Filament formation via the instability of a stretching viscous sheet: Physical mechanism, linear theory, and fiber applications, Phys. Rev. Fluids **4**, 073902 (2019).
[38] A. Javadi, J. Eggers, D. Bonn, M. Habibi, and N. M. Ribe, Delayed Capillary Breakup of Falling Viscous Jets, Phys. Rev. Lett. **110**, 144501 (2013).
[39] A. L. Andrew, E. K. Chu, and P. Lancaster, On the numerical solution of nonlinear eigenvalue problems, Computing **55**, 91 (1995).
[40] P. Guillaume, Nonlinear eigenproblems, SIAM J. Matrix Anal. Appl. **20**, 575 (1999).
[41] A. Ruhe, Rational Krylov for large nonlinear eigenproblems, Parallel computing **3732**, 357 (2004).

[42] H. Voss, A Jacobi-Davidson method for nonlinear and nonsymmetric eigenproblems, Comput. Structures **85**, 1284 (2007).
[43] B. Liao, Z. Bai, L. Lee, and K. Ko, Nonlinear Rayleigh-Ritz iterative method for solving large scale nonlinear eigenvalue problems, Taiwanese J. Mathematics **14**, 869 (2010).
[44] S. Tomotika, On the instability of a cylindrical thread of a viscous liquid surrounded by another viscous fluid, Proc. R. Soc. A **150**, 322 (1935).
[45] E. Anderson, Z. Bai, C. Bischof, L. S. Blackford, J. Demmel, J. Dongarra, J. Du Croz, A. Greenbaum, S. Hammarling, A. McKenney, and D. Sorensen, *LAPACK Users' Guide*, 3rd ed. (SIAM, Philadelphia, 1999), p. 1.
[46] G. I. Barenblatt, *Scaling* (Cambridge University, Cambridge, England, 2003).
[47] X. Liang, Modeling of fluids and waves with analytics and numerics, Ph.D. thesis, Massachusetts Institute of Technology, 2013.
[48] C. Mueller, V. Topolkaraev, D. Soerens, A. Hiltner, and E. Baer, Breathable polymer films produced by the microlayer coextrusion process, J. Appl. Polymer Sci. **78**, 816 (2000).
[49] M. Ponting, T. M. Burt, L. T. J. Korley, J. Andrews, A. Hiltner, and E. Baer, Gradient multilayer films by forced assembly coextrusion, Ind. Eng. Chem. Res. **49**, 12111 (2010).
[50] G. Miquelard-garnier, A. Guinault, D. Fromonteil, S. Delalande, and C. Sollogoub, Dispersion of carbon nanotubes in polypropylene via multilayer coextrusion: Influence on the mechanical properties, Polymer **54**, 4290 (2013).
[51] T. Messin, N. Follain, A. Guinault, C. Sollogoub, V. Gaucher, N. Delpouve, and S. Marais, Structure and barrier properties of multinanolayered biodegradable PLA/PBSA films: Confinement effect via forced assembly coextrusion, Appl. Mater. Inte. **9**, 29101 (2017).
[52] A. M. Jordan, B. Lee, K. Kim, E. Ludtke, O. Lhost, S. A. Jaffer, F. S. Bates, and C. W. Macosko, Rheology of polymer multilayers: Slip in shear, hardening in extension, J. Rheol. **63**, 751 (2019).
[53] K. Ho, J. S. Lee, N. Viriyabanthorn, C. Sung, C. M. F. Barry, and J. L. Mead, Interfacial instabilities in multilayer extrusion, in *Proceedings of the 2004 NSTI Nanotechnology Conference and Trade Show, 2004* (CRC Press, Boca Raton, 2007), Vol. 3, p. 468.
[54] T. E. Bernal-Lara, R. Y. F. Liu, A. Hiltner, and E. Baer, Structure and thermal stability of polyethylene nanolayers, Polymer **46**, 3043 (2005).
[55] R. Adhikari, W. Lebek, R. Godehardt, S. Henning, G. H. Michler, E. Baer, and A Hiltner, Investigating morphology and deformation behavior of multilayered PC/PET composites, Polym. Adv. Technol. **16**, 95 (2005).
[56] Y. Lin, A. Hiltner, and E. Baer, A new method for achieving nanoscale reinforcement of biaxially oriented polypropylene film, Polymer **51**, 4218 (2010).
[57] Y. Zhu, A. Bironeau, F. Restagno, C. Sollogoub, and G. Miquelard-garnier, Kinetics of thin polymer film rupture: Model experiments for a better understanding of layer breakups in the multilayer coextrusion process, Polymer **90**, 156 (2016).
[58] G. Krausch, Dewetting at the interface between two immiscible polymers Dewetting at the interface between two immiscible polymers, J. Phys.: Condens. Matter **9**, 7741 (1997).
[59] C. Wang, G. Krausch, and M. Geoghegan, Dewetting at a polymer-polymer interface: Film thickness dependence, Langmuir **17**, 6269 (2001).